

Origins of the Pressure-Induced Phase Transition and Metallization in the Halide Perovskite (CH₃NH₃)PbI₃

Jung-Hoon Lee,* Adam Jaffe, Yu Lin, Hemamala I. Karunadasa, and Jeffrey B. Neaton*

Cite This: *ACS Energy Lett.* 2020, 5, 2174–2181

Read Online

ACCESS |



Metrics & More

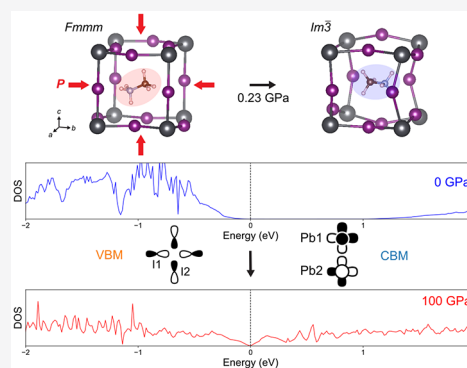


Article Recommendations



Supporting Information

ABSTRACT: Hybrid halide perovskites are promising for applications because of their favorable optoelectronic properties and low cost. Here we investigate the effects of hydrostatic pressure on the structural and electronic properties of (MA)PbI₃ (MA = CH₃NH₃⁺) using first-principles density functional theory calculations. Our calculations predict that at a pressure of 0.23 GPa, the orthorhombic *Fm* $\bar{3}$ *m* phase becomes unstable with respect to a cubic *Im* $\bar{3}$ phase, in good agreement with room-temperature experiments (\sim 0.3 GPa). At higher pressures, about 6 GPa, we predict the onset of pronounced intra- and interoctahedral distortions. This symmetry lowering leads to the introduction of I 5p–I 5p* antibonding and Pb 6p–Pb 6p bonding character into the valence band maximum (VBM) and the conduction band minimum (CBM) states, respectively. We find this change in bond character explains the evolution of the VBM and CBM states under compression, trends that ultimately lead to metallization at significantly higher pressures.



The application of hydrostatic pressure can induce significant changes to fundamental properties and promote the emergence of new properties and phenomena in materials that are not present under ambient conditions. In particular, laboratory-achievable pressures can induce structural phase transitions,^{1,2} amorphization,^{3–7} metallization,^{8,9} superconductivity,^{10–12} magnetic ordering,^{13,14} enhanced piezoelectricity,⁷ ferroelectricity,¹⁵ and metal–insulator transitions.¹⁶ Accordingly, studies of materials at high pressures provide fundamental insight into structural, optoelectronic, and magnetic properties of materials that can shed light on their performance in applications.

Lead-halide perovskites have been the subject of intense recent investigation for solar energy applications because of their strong absorption in the visible spectrum and long carrier diffusion lengths.^{17–20} Over the past decade, there has been a resurgence of interest in understanding their structural and electronic properties as a function of temperature and pressure. Previous experiments reported a range of behavior for halide perovskites under pressure, including pressure-induced phase transitions,^{21–30} amorphization,^{23–26,28} semiconductor–metal transitions,^{29,31–33} ferroelectricity,^{34,35} and topological order.^{34,36,37} In particular, in prior work the low-pressure α -phase of (MA)PbI₃, which has been reported as either tetragonal *I4/mcm* or orthorhombic *Fm* $\bar{3}$ *m*, has been observed to undergo a phase transition to an *Im* $\bar{3}$ cubic β -phase at room

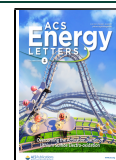
temperature near 0.3–0.4 GPa;^{23–25} separate work has also proposed the appearance of an *Imm2* orthorhombic phase at room temperature at 0.3 GPa.^{26,27} At somewhat higher pressures, an amorphous phase has been reported to appear around 2–3 GPa.^{23,25,27} Interestingly, this amorphous phase is reported to form reversibly, with the low-pressure crystalline phase recoverable upon decompression.²³ More interestingly, it was demonstrated that (MA)PbI₃ becomes metallic in its putative amorphous phase above 60 GPa.³⁸

Prior density functional theory (DFT) calculations of (MA)PbI₃ under pressure have successfully predicted band gap trends,^{23,24,26} despite the well-known quantitative shortcomings of DFT within common approximations for predicting gaps. Despite advances in prior work,^{23–27,29,34,38} an understanding of the structural and electronic origins of the pressure-induced phase transitions and structural changes that lead to metallization in (MA)PbI₃ is still lacking. In particular, the role of the MA ion in predicted pressure-induced phase transitions is not understood, and the observed nonmonotonic

Received: April 8, 2020

Accepted: May 18, 2020

Published: May 19, 2020



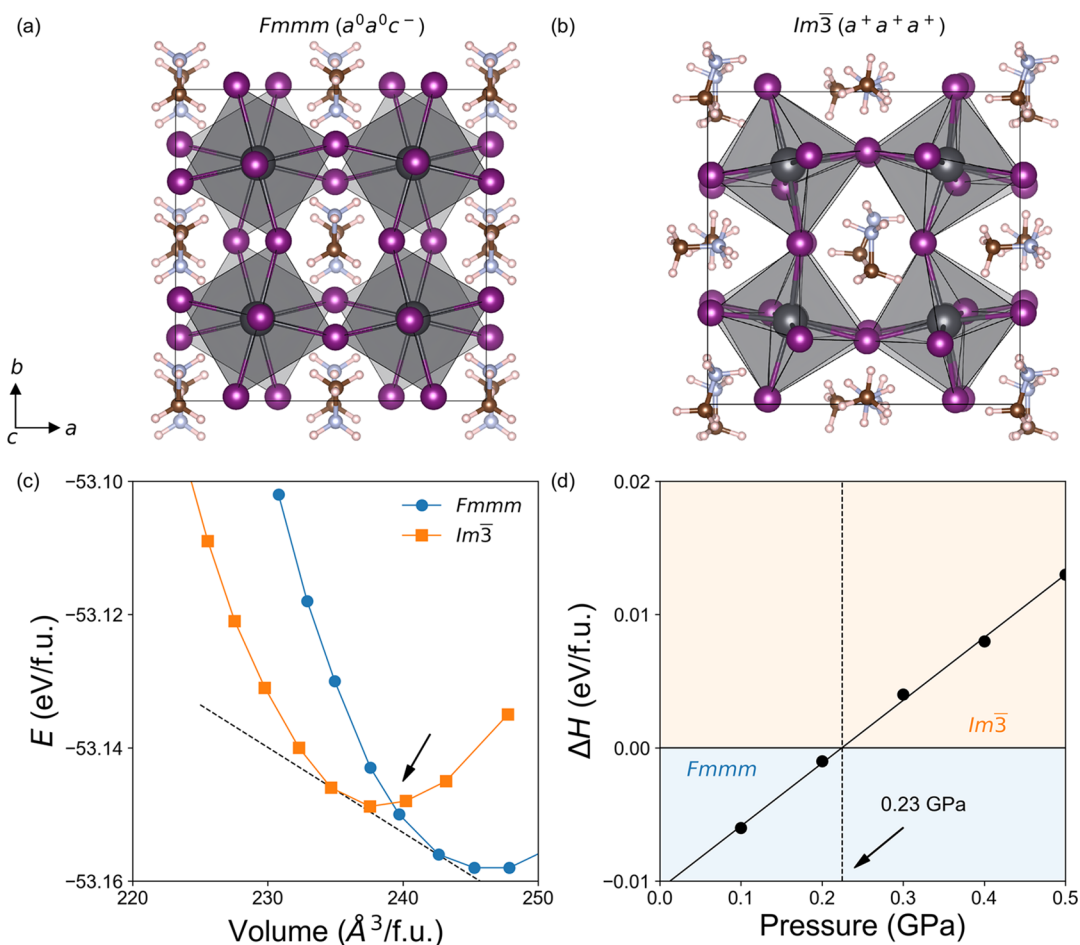


Figure 1. Optimized crystal structures of (MA)PbI₃ in the (a) orthorhombic $Fm\bar{m}m$ and (b) cubic $Im\bar{3}$ space groups. (c) DFT-PBE-SOC total energy (E) as a function of the volume per formula unit. A dotted line indicates the common tangent line between the $Fm\bar{m}m$ and $Im\bar{3}$ phases. We can see the energy crossover at 239 Å³/f.u. (black arrow). (d) Enthalpy difference (ΔH) between the $Fm\bar{m}m$ and $Im\bar{3}$ phases as a function of pressure. A dotted line indicates the enthalpy crossover at 0.23 GPa. We note that vibrational entropy changes are predicted to have only a small effect on the transition pressure (see Tables S1 and S2 and Figure S1 in the Supporting Information) and therefore are neglected in the calculations presented here.

band gap evolution³⁸ with pressure has yet to be explained. Here, we perform DFT calculations of (MA)PbI₃ under pressure, including spin-orbit coupling (SOC), and accurately predict the α - β phase transition pressure. In addition, our detailed calculations show that pronounced deviation from octahedral symmetry and interoctahedral tilting at 6 GPa dramatically alters the electronic structure of (MA)PbI₃, elucidating a potential route for eventual metallization at higher pressures.

In Figure 1a,b, we compare the structure of orthorhombic $Fm\bar{m}m$ (MA)PbI₃ with that of cubic $Im\bar{3}$ (MA)PbI₃ optimized with DFT at zero applied pressure. We use the generalized gradient approximation (PBE)³⁹ with SOC corrections for all DFT calculations. We use previous single-crystal X-ray diffraction studies²³ as a starting point in our structure relaxations (Figure S2). Experimental studies differ on the assignment of the ambient-pressure room-temperature phase of (MA)PbI₃, reporting an orthorhombic $Fm\bar{m}m$ ²³ phase or a tetragonal $I4cm$,⁴⁰ $I4/mcm$,²⁰ or $I4/m$ ⁴¹ phase. According to our DFT calculations, the orthorhombic and tetragonal phases are nearly degenerate: the tetragonal structure is merely 1 meV per formula unit (f.u.) more stable than the orthorhombic structure, as shown in Figure S3b. Further, previous work²³ that accounts for twinning, systematic absences, and non-

ellipsoidal iodide electron density and that includes independent refinement of Pb-I bond distances recently proposed $Fm\bar{m}m$ as the (MA)PbI₃ room-temperature phase. On the basis of these considerations and the near degeneracy of the $Fm\bar{m}m$ and $I4/mcm$ phases, we focus on the orthorhombic $Fm\bar{m}m$ phase for all calculations at lower pressures in this work.

For all structural optimizations with DFT, we fully relax both internal coordinates and unit cell volumes. Calculated lattice parameters for the $Fm\bar{m}m$ and $Im\bar{3}$ phases are given in Table 1 and agree with the experimental values within $\pm 2.5\%$. In DFT optimizations of the MA ions in the PbI₃ inorganic frameworks, we use a two-step procedure. Starting with the experimentally determined MA ion orderings (see Figure S2), we first relax the MA ions holding the PbI₃ inorganic framework atoms fixed and using the experimental lattice parameters; with the MA ions initially optimized, we then fully relax all internal coordinates including the MA ions and the unit cell volumes. Using this approach, our DFT calculations successfully reproduce octahedral tilting patterns of the $Fm\bar{m}m$ and $Im\bar{3}$ phases, which correspond to $a^0a^0c^-$ and $a^+a^+a^+$ in Glazer notation,⁴² respectively (Figure 1a,b). Moreover, the optimized MA ordering we predict for the $Fm\bar{m}m$ phase is the same as the nonpolar structure discussed in a previous DFT

Table 1. Computed Lattice Parameters of the Orthorhombic $Fm\bar{3}m$ and the Cubic $Im\bar{3}$ Phases of (MA)PbI₃ Compared to the Experimental Values Obtained at 0 and 0.7 GPa,²³ Respectively

	$Fm\bar{3}m$		$Im\bar{3}$	
	this work	experiment	this work	experiment
a	12.326 Å	12.498 Å	12.370 Å	12.305 Å
b	12.346 Å	12.518 Å	12.403 Å	12.305 Å
c	12.897 Å	12.601 Å	12.388 Å	12.305 Å
α	88.828°	90°	90.015°	90°
β	90.199°	90°	90.209°	90°
γ	89.895°	90°	89.775°	90°

study on this perovskite.⁴³ For the $Im\bar{3}$ phase, we repeat the two-step procedure outlined above, noting there are two inequivalent MA sites at Wyckoff positions (0, 0, 0) and (0.5, 0, 0), as shown in Figure S2b in the Supporting Information (see also Figure 1b).²³ Comparing calculated energetics for both structures, we find that the $Im\bar{3}$ phase is unstable with respect to the $Fm\bar{3}m$ phase at zero applied pressure. However, the computed DFT-PBE-SOC energy difference between the two phases is 8 meV/f.u. Therefore, we might expect a phase transition occurring under relatively small external perturbations.

To investigate the possibility of a pressure-induced phase transition between the two structures, we relax the structures and compute the total energy (E) as a function of the unit cell volume for the $Fm\bar{3}m$ and $Im\bar{3}$ phases. The results are shown in Figure 1c, and indeed, our calculations predict a pressure-induced structural phase transition at 0.23 GPa from $Fm\bar{3}m$ to $Im\bar{3}$, obtained from a common tangent line marked with a dotted line in Figure 1c. Even though the enthalpy difference between two phases is very small, we can clearly see a crossover in ΔH with increasing pressure (Figure 1d). Notably, our prediction agrees well with the experimental value of ~ 0.3 GPa.²³

We perform a series of calculations to show that the MA cation arrangement plays a critical role in the phase transition at 0.23 GPa. Figure 2 summarizes the computed MA binding energy per MA cation as a function of unit cell volume for different MA cation orderings. Here, we define the MA binding

energy, MA E_B , as the energy required to remove all MA cations (or one MA cation) from a unit cell, holding the PbI₃ framework fixed, i.e., $E_B = E((MA)PbI_3) - E(MA) - E(PbI_3^-)$. In computing $E(MA)$, we use a large supercell and perform a single-point DFT calculation of an isolated MA molecule, keeping the coordinates fixed to those in (MA)PbI₃ at a given volume; in our calculations, we remove a charge from the system and include a uniform compensating background. In computing $E(PbI_3^-)$, we consider a rigid PbI₃ framework in each case, keeping the coordinates fixed to those in (MA)PbI₃ at a given volume; we add a charge to this system and include a uniform compensating background.

In Figure 2a, the computed MA E_B of the optimized $Fm\bar{3}m$ and $Im\bar{3}$ phases are shown to crossover with compression (indicated by a dotted line), with the MA E_B of the $Im\bar{3}$ phase becoming more stable than that of the $Fm\bar{3}m$ phase at higher pressure. Interestingly, the crossover volume 236 Å³/f.u. (dotted line in Figure 2a) is very similar to the phase transition volume 239 Å³/f.u. (black arrow in Figure 1c) indicated in Figure 1c, suggesting that the $Im\bar{3}$ inorganic framework becomes more favorable for MA cations than that of $Fm\bar{3}m$ under pressure. Figure 2a shows the optimized ordering, consistent with Figure 1c. In Figure 2b,c, we show computed energetics for the cases when MA cations are arranged to align in parallel (Ferro-MA ordering) and antiparallel (Antiferro-MA ordering). In both of these cases, neither a MA binding energy crossover nor a pressure-induced phase transition is computed to occur (Figures S5 and S6). According to our calculations, the MA binding energy is not simply determined by hydrogen-bonding interactions. In Figure S7, we show that the computed N–H⋯I hydrogen bond length, a proxy for hydrogen bond strength, does not trend with the energetics in Figure 2. Further studies exploring the origin of the MA binding energy change under pressure in more detail would be desirable. As shown in the Supporting Information, we additionally perform calculations of the two phases after replacing the MA cation with Cs⁺. Steric effects are invoked in relative stability arguments between crystal structures. However, in previous DFT calculations on halide perovskites,⁴⁴ interactions between the MA cations and the inorganic framework were shown to play a more critical role in stabilizing the crystal structures of halide perovskites (such as

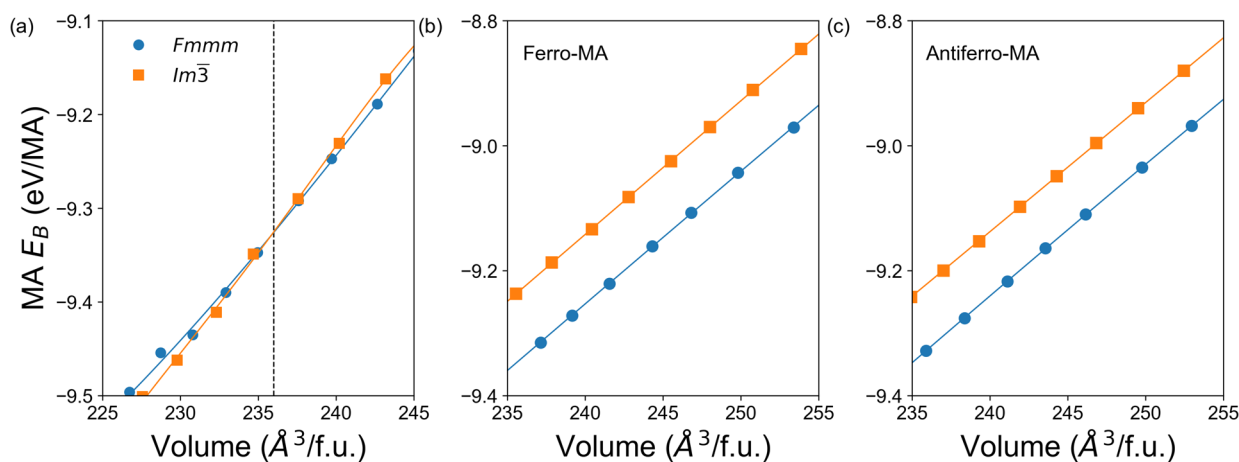


Figure 2. Computed MA binding energy per MA cation (MA E_B) as a function of volume for (a) the optimized MA ordering shown in Figure 1a,b, (b) the parallel-aligned MA cation (Ferro-MA ordering), and (c) the antiparallel-aligned MA cation (Antiferro-MA ordering) cases. A dotted line in panel a indicates the volume at the crossover.

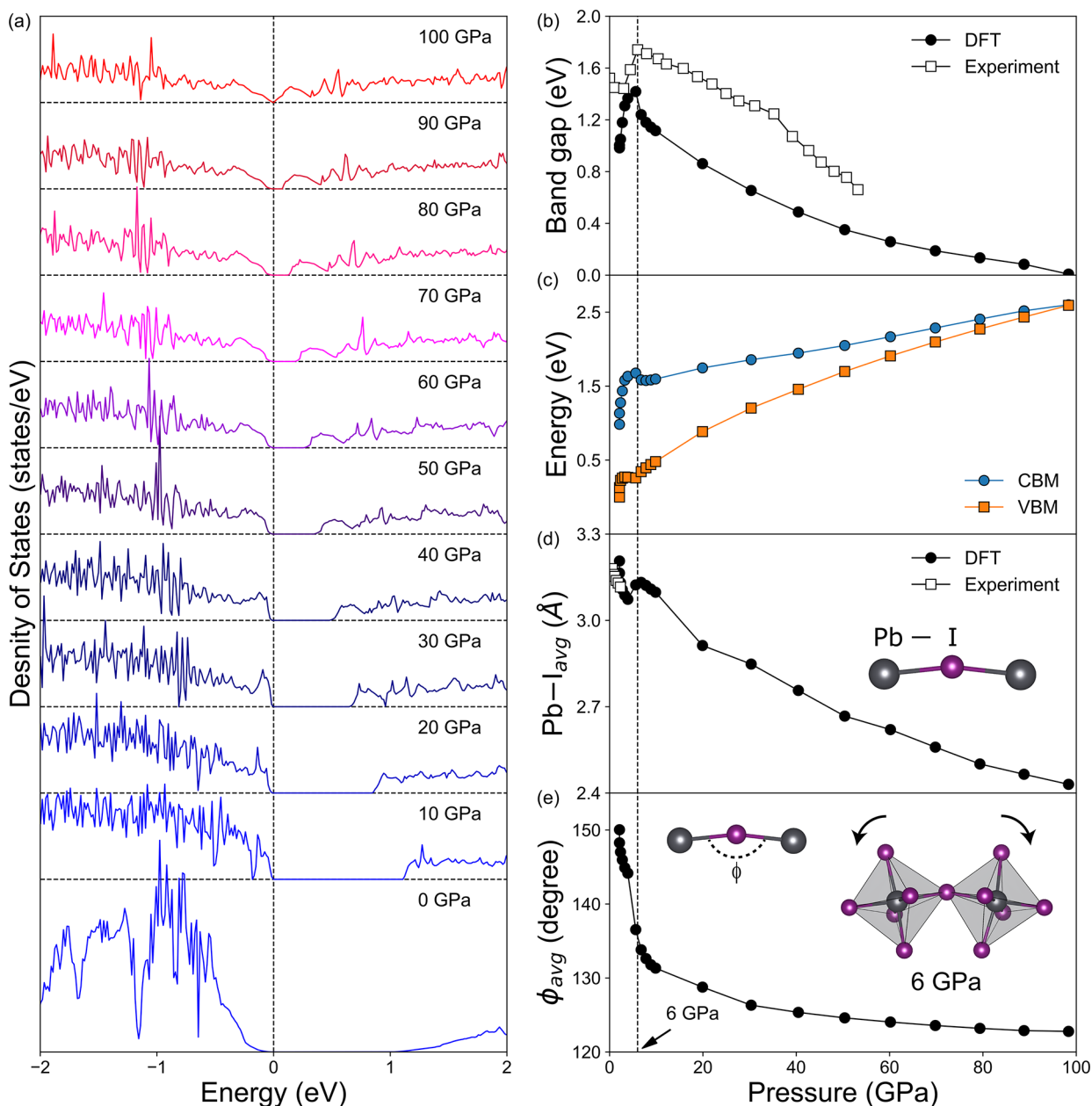


Figure 3. (a) Total density of states (DOS) of the $Im\bar{3}$ phase for different pressures. Zero energy corresponds to the valence band maximum (VBM) position. (b) The band gaps, (c) valence band maximum (VBM) and conduction band minimum (CBM) positions, (d) average Pb–I distance ($Pb-I_{avg}$), and (e) average Pb–I–Pb angle (ϕ_{avg}) of the $Im\bar{3}$ phase are shown as a function of pressure. The experimental values are obtained from ref 23.

(MA)PbI₃) than size effects at zero pressure. Moreover, the high-pressure $Im\bar{3}$ structure has two different A sites (see Figure S2b). As we pointed out in ref 23, this structure is usually adopted by perovskites that contain two different A-site cations. Hence, a key difference between MA and Cs⁺ is that MA can disorder differently and occupy the two different A sites in the $Im\bar{3}$ structure. Cs⁺ cannot do this as a spherical ion. Thus, it is appropriate to replace the MA cation with Cs⁺ to see the role of interactions between the MA cations and the Pb–I inorganic framework in the phase stability of (MA)PbI₃ under pressure. We find that this inorganic lattice does not exhibit a phase transition at a similar pressure (Figure S8). Hence, we can conclude that specific interactions between the MA cations and the Pb–I inorganic framework are critical in determining the phase stability of (MA)PbI₃ under pressure. Even though

the MA cations are relatively disordered compared to the Pb–I inorganic framework at room temperature, the different symmetry-inequivalent MA cations are measured to exhibit different degrees of disorder, as shown in the X-ray diffraction data in Figure S2; given the presence of some order, we still expect our conclusions to be relevant. Moreover, according to previous phonon calculations,⁴⁵ soft phonon modes in the 0–50 cm⁻¹ (=0–6.2 meV) energy range correspond to correlated phonons of the MA cations and the Pb–I inorganic framework. In other words, these phonon modes, which are a measure of interactions between the MA cations and the Pb–I inorganic framework, are likely to harden under pressure, further ordering the MA cations. Thus, the optimized MA orderings shown in Figure 1a,b are expected to be dynamically sampled at room temperature.

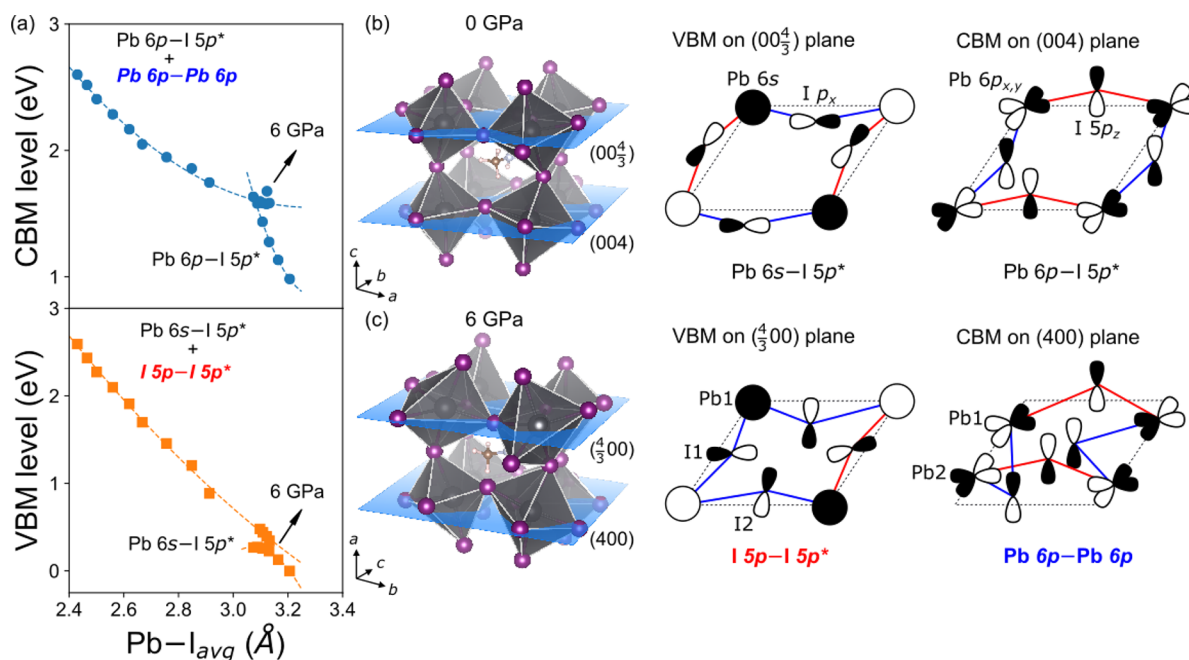


Figure 4. (a) VBM and CBM energies of the high-pressure phase as a function of Pb–I_{avg}, referenced to the I 1s core level. Dotted lines correspond to the extrapolated trend lines separately obtained from 0–5 GPa and 7–100 GPa regions. Structures and the orbital interaction diagrams of the VBM and CBM bands at (b) 0 GPa and (c) 6 GPa. The orbital interaction diagrams of the VBM and CBM bands are obtained on (00 $\frac{4}{3}$) and (004) planes, respectively, for 0 GPa and on ($\frac{4}{3}$ 00) and (400), respectively, for 6 GPa. These planes are indicated in the crystal structures. Red and blue lines indicate Pb–I bonds above and below the planes, respectively. The corresponding wave function contours of the VBM and CBM bands are shown in Figure S14 in the Supporting Information.

Next, we examine pathways to metallization by starting with the cubic $Im\bar{3}$ unit cell and compressing the volume to simulate pressures up to 100 GPa. Our optimized lattice parameters and unit cell volumes of $Im\bar{3}$ are in good agreement with the experiment values up to 48.5 GPa²³ as shown in Figure S9, although we see symmetry-lowering structural distortions as a function of pressure (discussed below). Figure 3a shows the total density of states (DOS) of this high-pressure phase for different pressures. The band structures are shown in Figure S10. At equilibrium volume, the computed DFT band gap of the high-pressure phase is 0.98 eV, underestimating the experimental band gap by ~ 0.5 eV. Although DFT-PBE is well-known to underestimate the band gap of semiconductors,^{46–49} we can expect qualitative trends to be meaningful, as has been shown in some previous DFT studies.^{50,51}

We note that our metallization pressure (100 GPa) overestimates the experimental value of 60 GPa;³⁸ further, we do not predict the onset of a more rapidly decreasing band gap above 35 GPa reported in a prior experiment.³⁸ We attribute these differences to the fact that, at these elevated pressures, our optimized structures deviate from those in room-temperature experiments. For example, above ~ 3 GPa, (MA)PbI₃ is known to become partially amorphous.²³ While some diffraction peaks from the $Im\bar{3}$ phase remain at higher pressures, such as the (200) reflection, a large degree of amorphous character was observed in the diffraction patterns where the structure is unknown. The behavior of the amorphous structure could lead to differences in atomic positions and electronic structure and therefore different metallization pressures. Severe changes in structure could also lead to defects lying close to the VBM or CBM in the band gap. With a high defect density and subsequent thermal promotion of defect-derived carriers to the valence or

conduction bands, metallic or semimetallic character could be induced—potentially at a lower pressure than the band gap closure expected for a defect-free crystal. Finally, because compression is no longer hydrostatic at the higher pressures reached by prior experimental studies, local stresses may exceed the sample average and could lead to anomalously early metallization as a function of higher local pressure on certain domains or grain boundaries.^{38,52} Further study of the partially amorphous high-pressure (MA)PbI₃ phase as well as assessment of any pressure-induced defects may be necessary to fully explain the nature of its metallization.

Interestingly, the predicted change in the evolution of the band gap energy under pressure, at ~ 6 GPa, is strongly correlated with the increasing amplitude of structural distortions. From Figures 3d,e, 4a, S11, and S12, a large distortion including both intra- and inter(tilting)octahedral distortions occurs at 6 GPa, reminiscent of a phase transition. These distortions are illustrated in Figures 3e (inset) and S12a. In general, the average Pb–I–Pb angle (ϕ_{avg}) decreases with increasing pressure (Figure 3e). However, ϕ_{avg} exhibits a more significant decrease from 144.1° to 136.5° at 6 GPa. Moreover, the average deviation (θ_{avg}) from the perfect I–Pb–I angle (90°) within the octahedra significantly increases from 8.8° to 14.0° at 6 GPa (see Figure S12). Concomitant with this sudden increase in degree of octahedral distortion from 5 to 6 GPa, the average Pb–I bond length (Pb–I_{avg}) increases from 3.07 to 3.12 Å (Figure 3d) but then decreases with subsequent compression. The significant intra- and interoctahedral distortions occurring at 6 GPa alter the electronic properties of (MA)PbI₃, leading to eventual metallization, as we describe below.

To understand the nonmonotonic trends in band gap and in the VBM and CBM energies, we note that the bond length

Pb–I_{avg} decreases by ~22% between 6 and 100 GPa (Figure 3d) compared with only a ~10% change in ϕ_{avg} over the same range (Figure 3e). As both the VBM and CBM states consist of antibonding and nonbonding orbital characters, the Pb–I bond length shortening generally destabilizes both states (Figure 4a). However, at 6 GPa we observe different trends in VBM and CBM energies, indicating that the octahedral distortion at 6 GPa alters the electronic structure of the high-pressure phase of (MA)PbI₃. At equilibrium volume, the VBM and CBM states of (MA)PbI₃ are mainly composed of Pb 6s–I 5p* and Pb 6p–I 5p* antibonding interactions, respectively, as shown in Figures 4b, S13, and S14a.⁴⁴ However, a dramatic change in octahedral distortion at 6 GPa introduces additional antibonding and bonding orbital interactions. At the VBM, previously nonbonding I 5p orbitals begin to interact with each other to form antibonding I 5p–I 5p* orbitals at 6 GPa (see partial density of states in Figure S13 and wave function contours in Figure S14b), adding to the existing antibonding character of the Pb 6s–I 5p* interactions above that pressure.

In the case of the CBM state, the severe octahedral distortion induces Pb 6p–Pb 6p bonding interactions (Figures 4c, S13d,e, and S14b), as the structural distortion moves the iodide atom that bridges Pb1 and Pb2 away from the (400) plane containing Pb1 and Pb2, although the 4.6 Å distance between Pb atoms suggests a weak interaction. The presence of both antibonding Pb 6p–I 5p* and bonding Pb 6p–Pb 6p interactions in the CBM above 6 GPa leads to a different energetic trend with pressure from that of the VBM state. In Figures 3c, 4a, and S11, we can clearly see that the Pb 6p–Pb 6p bonding interaction stabilizes—or rather hinders destabilization—of the CBM state above 6 GPa. Conversely, the VBM state displays a strong destabilization trend, as it is primarily composed of antibonding interactions. The different trends in VBM and CBM energies, associated with different degree of destabilization with pressure, reduce the band gap with compression, until the gap finally closes at a predicted 100 GPa for the high-pressure phase (Figures 3 and S10). Thus, we conclude the additional orbital interactions (I 5p–I 5p* antibonding and Pb 6p–Pb 6p bonding interactions) introduced by the significant octahedral distortion at 6 GPa are responsible for the eventual metallization of (MA)PbI₃.

In conclusion, we have examined the origins of the pressure-induced α -to- β phase transition and subsequent metallization in (MA)PbI₃. Our DFT calculations, including SOC, accurately predict the measured pressure-induced phase transition from *Fm* $\bar{3}$ m to *Im* $\bar{3}$. In addition, we show that this transition originates from the enhanced stability of the MA cation in the *Im* $\bar{3}$ inorganic framework relative to the *Fm* $\bar{3}$ m inorganic framework under pressure. We further showed that changes in bonding character of the VBM and CBM states under pressure, owing to intra- and interoctahedral distortions, can lead to eventual metallization of (MA)PbI₃ at higher pressures. Further experimental investigation of the high-pressure structure and electronic properties of (MA)PbI₃ and related halide perovskites would be of interest to corroborate the predictions made here.

■ ASSOCIATED CONTENT

SI Supporting Information

The Supporting Information is available free of charge at <https://pubs.acs.org/doi/10.1021/acsenerylett.0c00772>.

Computational methods, entropy contribution, experimental crystal structures, comparison of the orthorhombic *Fm* $\bar{3}$ m structure to the tetragonal *I4/mcm* structure, enthalpies and hydrogen bond distances as a function of pressure for different MA cation orderings and CsPbI₃, lattice parameters of the *Im* $\bar{3}$ phase as a function of pressure, band structures, band edge positions versus average Pb–I–Pb angle, intraoctahedral distortion as a function of pressure, partial density of states, and wave function contours (PDF)

■ AUTHOR INFORMATION

Corresponding Authors

Jung-Hoon Lee – Molecular Foundry, Lawrence Berkeley National Laboratory, Berkeley, California 94720, United States; Department of Physics, University of California, Berkeley, California 94720, United States; Computational Science Research Center, Korea Institute of Science and Technology, Seoul 02792, Republic of Korea; orcid.org/0000-0002-2983-678X; Email: jhlee84@kist.re.kr

Jeffrey B. Neaton – Molecular Foundry, Lawrence Berkeley National Laboratory, Berkeley, California 94720, United States; Department of Physics, University of California, Berkeley, California 94720, United States; Kavli Energy Nanosciences Institute at Berkeley, Berkeley, California 94720, United States; Email: jbneaton@lbl.gov

Authors

Adam Jaffe – Department of Chemistry, Stanford University, Stanford, California 94305, United States; orcid.org/0000-0002-9886-0249

Yu Lin – Stanford Institute for Materials and Energy Sciences, SLAC National Accelerator Laboratory, Menlo Park, California 94025, United States; orcid.org/0000-0001-5174-9546

Hemamala I. Karunadasa – Department of Chemistry, Stanford University, Stanford, California 94305, United States; Stanford Institute for Materials and Energy Sciences, SLAC National Accelerator Laboratory, Menlo Park, California 94025, United States; orcid.org/0000-0003-4949-8068

Complete contact information is available at: <https://pubs.acs.org/doi/10.1021/acsenerylett.0c00772>

Notes

The authors declare no competing financial interest.

■ ACKNOWLEDGMENTS

We thank Sehoon Oh at UC Berkeley for helpful discussions. This work was supported by the Department of Energy, Office of Basic Energy Sciences, Division of Materials Sciences and Engineering (Theory FWP), under contract No. DE-AC02-05CH11231. Computational resources used at the Molecular Foundry were supported by the Department of Energy, Office of Basic Energy Sciences, under contract No. DE-AC02-05CH11231; additional computational resources were provided by NERSC. This research also used the Savio computational cluster resource provided by the Berkeley Research Computing program at the University of California, Berkeley (supported by the UC Berkeley Chancellor, Vice Chancellor for Research, and Chief Information Officer). A.J. is grateful for the Stanford Interdisciplinary Graduate Fellowship and the William S. Johnson Fellowship from the Stanford Department of Chemistry. Work by Y.L. and H.I.K. was

supported through the Department of Energy, Office of Basic Energy Sciences, Division of Materials Sciences and Engineering, under contract DE-AC02-76SF00515.

REFERENCES

- (1) Minomura, S.; Drickamer, H. Pressure induced phase transitions in silicon, germanium and some III–V compounds. *J. Phys. Chem. Solids* **1962**, *23*, 451–456.
- (2) Cohen, A. J.; Gordon, R. G. Theory of the lattice energy, equilibrium structure, elastic constants, and pressure-induced phase transitions in alkali-halide crystals. *Phys. Rev. B* **1975**, *12*, 3228–3241.
- (3) Hemley, R. J.; Jephcoat, A. P.; Mao, H. K.; Ming, L. C.; Manghni, M. H. Pressure-induced amorphization of crystalline silica. *Nature* **1988**, *334*, 52–54.
- (4) Vannereau, F.; Itié, J. P.; Polian, A.; Calas, G.; Petiau, J.; Fontaine, A.; Tolentino, H. Pressure-induced coordination changes of germanium in crystalline and vitreous germanates. *High Pressure Res.* **1991**, *7*, 372–374.
- (5) Perottoni, C. A.; da Jornada, J. A. H. Pressure-induced amorphization and negative thermal expansion in ZrW_2O_8 . *Science* **1998**, *280*, 886–889.
- (6) Deb, S. K.; Wilding, M.; Somayazulu, M.; McMillan, P. F. Pressure-induced amorphization and an amorphous–amorphous transition in densified porous silicon. *Nature* **2001**, *414*, 528–530.
- (7) Wu, Z.; Cohen, R. E. Pressure-induced anomalous phase transitions and colossal enhancement of piezoelectricity in $PbTiO_3$. *Phys. Rev. Lett.* **2005**, *95*, 037601.
- (8) Wei, S. H.; Krakauer, H. Local-density-functional calculation of the pressure-induced metallization of BaSe and BaTe. *Phys. Rev. Lett.* **1985**, *55*, 1200–1203.
- (9) Zhao, Z.; Zhang, H.; Yuan, H.; Wang, S.; Lin, Y.; Zeng, Q.; Xu, G.; Liu, Z.; Solanki, G. K.; Patel, K. D.; Cui, Y.; Hwang, H. Y.; Mao, W. L. Pressure induced metallization with absence of structural transition in layered molybdenum diselenide. *Nat. Commun.* **2015**, *6*, 7312.
- (10) Kimura, N.; Ito, K.; Saitoh, K.; Umeda, Y.; Aoki, H.; Terashima, T. Pressure-induced superconductivity in noncentrosymmetric heavy-fermion $CeRhSi_3$. *Phys. Rev. Lett.* **2005**, *95*, 247004.
- (11) Torikachvili, M. S.; Bud'ko, S. L.; Ni, N.; Canfield, P. C. Pressure induced superconductivity in $CaFe_2As_2$. *Phys. Rev. Lett.* **2008**, *101*, 057006.
- (12) Drozdov, A. P.; Eremets, M. I.; Troyan, I. A.; Ksenofontov, V.; Shylin, S. I. Conventional superconductivity at 203 K at high pressures in the sulfur hydride system. *Nature* **2015**, *525*, 73–76.
- (13) Egan, L.; Kamenev, K.; Papanikolaou, D.; Takabayashi, Y.; Margadonna, S. Pressure induced sequential magnetic pole inversion and antiferromagnetic-ferromagnetic crossover in a trimetallic Prussian blue analogue. *J. Am. Chem. Soc.* **2006**, *128*, 6034–6035.
- (14) Ding, Y.; Haskel, D.; Ovchinnikov, S. G.; Tseng, Y. C.; Orlov, Y. S.; Lang, J. C.; Mao, H. K. Novel pressure-induced magnetic transition in magnetite (Fe_3O_4). *Phys. Rev. Lett.* **2008**, *100*, 045508.
- (15) dela Cruz, C. R.; Lorenz, B.; Sun, Y. Y.; Wang, Y.; Park, S.; Cheong, S.-W.; Gospodinov, M. M.; Chu, C. W. Pressure-induced enhancement of ferroelectricity in multiferroic RMn_2O_5 ($R = Tb, Dy, Ho$). *Phys. Rev. B: Condens. Matter Mater. Phys.* **2007**, *76*, 174106.
- (16) Neaton, J. B.; Ashcroft, N. W. Pairing in dense lithium. *Nature* **1999**, *400*, 141–144.
- (17) Liu, M.; Johnston, M. B.; Snaith, H. J. Efficient planar heterojunction perovskite solar cells by vapour deposition. *Nature* **2013**, *501*, 395–398.
- (18) Snaith, H. J. Perovskites: the emergence of a new era for low-cost, high-efficiency solar cells. *J. Phys. Chem. Lett.* **2013**, *4*, 3623–3630.
- (19) Kim, H.-S.; Lee, C.-R.; Im, J.-H.; Lee, K.-B.; Moehl, T.; Marchioro, A.; Moon, S.-J.; Humphry-Baker, R.; Yum, J.-H.; Moser, J. E.; Grätzel, M.; Park, N.-G. Lead iodide perovskite sensitized all-solid-state submicron thin film mesoscopic solar cell with efficiency exceeding 9%. *Sci. Rep.* **2012**, *2*, 591.
- (20) Baikie, T.; Fang, Y.; Kadro, J. M.; Schreyer, M.; Wei, F.; Mhaisalkar, S. G.; Grätzel, M.; White, T. J. Synthesis and crystal chemistry of the hybrid perovskite $(CH_3NH_3)PbI_3$ for solid-state sensitized solar cell applications. *J. Mater. Chem. A* **2013**, *1*, 5628–5641.
- (21) Matsuishi, K.; Ishihara, T.; Onari, S.; Chang, Y. H.; Park, C. H. Optical properties and structural phase transitions of lead-halide based inorganic-organic 3D and 2D perovskite semiconductors under high pressure. *Phys. Status Solidi B* **2004**, *241*, 3328–3333.
- (22) Swainson, I. P.; Tucker, M. G.; Wilson, D. J.; Winkler, B.; Milman, V. Pressure response of an organic-inorganic perovskite: methylammonium lead bromide. *Chem. Mater.* **2007**, *19*, 2401–2405.
- (23) Jaffe, A.; Lin, Y.; Beavers, C. M.; Voss, J.; Mao, W. L.; Karunadasa, H. I. High-pressure single-crystal structures of 3D lead-halide hybrid perovskites and pressure effects on their electronic and optical properties. *ACS Cent. Sci.* **2016**, *2*, 201–209.
- (24) Jiang, S.; Fang, Y.; Li, R.; Xiao, H.; Crowley, J.; Wang, C.; White, T. J.; Goddard, W. A.; Wang, Z.; Baikie, T.; Fang, J. Pressure-dependent polymorphism and band-gap tuning of methylammonium lead iodide perovskite. *Angew. Chem., Int. Ed.* **2016**, *55*, 6540–6544.
- (25) Szafranski, M.; Katrusiak, A. Mechanism of pressure-induced phase transitions, amorphization, and absorption-edge shift in photovoltaic methylammonium lead iodide. *J. Phys. Chem. Lett.* **2016**, *7*, 3458–3466.
- (26) Kong, L.; Liu, G.; Gong, J.; Hu, Q.; Schaller, R. D.; Dera, P.; Zhang, D.; Liu, Z.; Yang, W.; Zhu, K.; Tang, Y.; Wang, C.; Wei, S.-H.; Xu, T.; Mao, H.-k. Simultaneous band-gap narrowing and carrier-lifetime prolongation of organic-inorganic trihalide perovskites. *Proc. Natl. Acad. Sci. U. S. A.* **2016**, *113*, 8910–8915.
- (27) Capitani, F.; Marini, C.; Caramazza, S.; Postorino, P.; Garbarino, G.; Hanfland, M.; Pisanu, A.; Quadrelli, P.; Malavasi, L. High-pressure behavior of methylammonium lead iodide ($MAPbI_3$) hybrid perovskite. *J. Appl. Phys.* **2016**, *119*, 185901.
- (28) Wang, T.; Daiber, B.; Frost, J. M.; Mann, S. A.; Garnett, E. C.; Walsh, A.; Ehrler, B. Indirect to direct bandgap transition in methylammonium lead halide perovskite. *Energy Environ. Sci.* **2017**, *10*, 509–515.
- (29) Jaffe, A.; Lin, Y.; Karunadasa, H. I. Halide perovskites under pressure: accessing new properties through lattice compression. *ACS Energy Lett.* **2017**, *2*, 1549–1555.
- (30) Zhu, H.; Cai, T.; Que, M.; Song, J.-P.; Rubenstein, B. M.; Wang, Z.; Chen, O. Pressure-induced phase transformation and band-gap engineering of formamidinium lead iodide perovskite nanocrystals. *J. Phys. Chem. Lett.* **2018**, *9*, 4199–4205.
- (31) Lü, X.; Yang, W.; Jia, Q.; Xu, H. Pressure-induced dramatic changes in organic-inorganic halide perovskites. *Chem. Sci.* **2017**, *8*, 6764–6776.
- (32) Zhang, L.; Liu, C.; Wang, L.; Liu, C.; Wang, K.; Zou, B. Pressure-induced emission enhancement, band-gap narrowing, and metallization of halide perovskite $Cs_3Bi_2I_9$. *Angew. Chem., Int. Ed.* **2018**, *57*, 11213–11217.
- (33) Huang, Y.; Wang, L.; Ma, Z.; Wang, F. Pressure-induced band structure evolution of halide perovskites: a first-principles atomic and electronic structure study. *J. Phys. Chem. C* **2019**, *123*, 739–745.
- (34) Liu, S.; Kim, Y.; Tan, L. Z.; Rappe, A. M. Strain-induced ferroelectric topological insulator. *Nano Lett.* **2016**, *16*, 1663–1668.
- (35) Zhao, Y.-Q.; Ma, Q.-R.; Liu, B.; Yu, Z.-L.; Cai, M.-Q. Pressure-induced strong ferroelectric polarization in tetra-phase perovskite $CsPbBr_3$. *Phys. Chem. Chem. Phys.* **2018**, *20*, 14718–14724.
- (36) Jin, H.; Im, J.; Freeman, A. J. Topological insulator phase in halide perovskite structures. *Phys. Rev. B: Condens. Matter Mater. Phys.* **2012**, *86*, 121102.
- (37) Kashikar, R.; Khamari, B.; Nanda, B. R. K. Second-neighbor electron hopping and pressure induced topological quantum phase transition in insulating cubic perovskites. *Phys. Rev. Mater.* **2018**, *2*, 124204.
- (38) Jaffe, A.; Lin, Y.; Mao, W. L.; Karunadasa, H. I. Pressure-induced metallization of the halide perovskite $(CH_3NH_3)PbI_3$. *J. Am. Chem. Soc.* **2017**, *139*, 4330–4333.

- (39) Perdew, J. P.; Burke, K.; Ernzerhof, M. Generalized gradient approximation made simple. *Phys. Rev. Lett.* **1996**, *77*, 3865–3868.
- (40) Stoumpos, C. C.; Malliakas, C. D.; Kanatzidis, M. G. Semiconducting tin and lead iodide perovskites with organic cations: phase transitions, high mobilities, and near-infrared photoluminescent properties. *Inorg. Chem.* **2013**, *52*, 9019–9038.
- (41) Saidaminov, M. I.; Abdelhady, A. L.; Murali, B.; Alarousu, E.; Burlakov, V. M.; Peng, W.; Dursun, I.; Wang, L.; He, Y.; Maculan, G.; Goriely, A.; Wu, T.; Mohammed, O. F.; Bakr, O. M. High-quality bulk hybrid perovskite single crystals within minutes by inverse temperature crystallization. *Nat. Commun.* **2015**, *6*, 7586.
- (42) Glazer, A. M. The classification of tilted octahedra in perovskites. *Acta Crystallogr., Sect. B: Struct. Crystallogr. Cryst. Chem.* **1972**, *28*, 3384–3392.
- (43) Liu, S.; Zheng, F.; Grinberg, I.; Rappe, A. M. Photoferroelectric and photopiezoelectric properties of organometal halide perovskites. *J. Phys. Chem. Lett.* **2016**, *7*, 1460–1465.
- (44) Lee, J.-H.; Bristowe, N. C.; Lee, J. H.; Lee, S.-H.; Bristowe, P. D.; Cheetham, A. K.; Jang, H. M. Resolving the physical origin of octahedral tilting in halide perovskites. *Chem. Mater.* **2016**, *28*, 4259–4266.
- (45) Motta, C.; El-Mellouhi, F.; Kais, S.; Tabet, N.; Alharbi, F.; Sanvito, S. Revealing the role of organic cations in hybrid halide perovskite $\text{CH}_3\text{NH}_3\text{PbI}_3$. *Nat. Commun.* **2015**, *6*, 7026.
- (46) Perdew, J. P.; Zunger, A. Self-interaction correction to density-functional approximations for many-electron systems. *Phys. Rev. B: Condens. Matter Mater. Phys.* **1981**, *23*, 5048–5079.
- (47) Perdew, J. P.; Parr, R. G.; Levy, M.; Balduz, J. L. Density-functional theory for fractional particle number: derivative discontinuities of the energy. *Phys. Rev. Lett.* **1982**, *49*, 1691–1694.
- (48) Perdew, J. P.; Levy, M. Physical content of the exact Kohn-Sham orbital energies: band gaps and derivative discontinuities. *Phys. Rev. Lett.* **1983**, *51*, 1884–1887.
- (49) Sham, L. J.; Schlüter, M. Density-functional theory of the energy gap. *Phys. Rev. Lett.* **1983**, *51*, 1888–1891.
- (50) Khairallah, S. A.; Militzer, B. First-principles studies of the metallization and the equation of state of Solid helium. *Phys. Rev. Lett.* **2008**, *101*, 106407.
- (51) Ramzan, M.; Lebègue, S.; Ahuja, R. Electronic structure and metalization of a silane-hydrogen system under high pressure investigated using density functional and GW calculations. *Phys. Rev. B: Condens. Matter Mater. Phys.* **2010**, *81*, 233103.
- (52) Zhuang, Y.; Dai, L.; Li, H.; Hu, H.; Liu, K.; Yang, L.; Pu, C.; Hong, M.; Liu, P. Deviatoric stresses promoted metallization in rhenium disulfide. *J. Phys. D: Appl. Phys.* **2018**, *51*, 165101.